

Highly Ordered Gold Nanopatterned Indium Tin Oxide Electrodes for Simultaneous Optical and Electrochemical Probing Cell Interactions

Diego Pallarola,^{*,†} Alexander Bochen,[‡] Victoria Guglielmotti,[†] Tabea A. Oswald,^{§,⊥} Horst Kessler,[‡] and Joachim P. Spatz^{§,⊥}

[†]Instituto de Nanosistemas, Universidad Nacional de General San Martín, Av. 25 de Mayo y Francia, San Martín 1650, Argentina

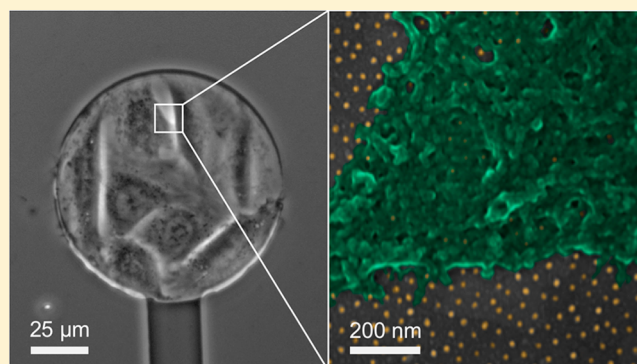
[‡]Department of Chemistry, Institute for Advanced Study and Center for Integrated Protein Science, Technische Universität München, Lichtenbergstr. 4, 85747 Garching, Germany

[§]Department of Cellular Biophysics, Max-Planck-Institute for Medical Research, Heisenbergstr. 3, 70569 Stuttgart, Germany

[⊥]Department of Biophysical Chemistry, Institute of Physical Chemistry, Heidelberg University, 69120 Heidelberg, Germany

Supporting Information

ABSTRACT: The formation of new types of sensitive conductive surfaces for the detection and transduction of cell–extracellular matrix recognition events in a real time, label-free manner is of great interest in the field of biomedical research. To study molecularly defined cell functions, biologically inspired materials that mimic the nanoscale order of extracellular matrix protein fibers and yield suitable electrical charge transfer characteristics are highly desired. Our strategy to achieve this goal is based on the spatial self-organization of patches of cell-adhesive molecules onto a gold-nanoparticle-patterned indium tin oxide electrode. Fibroblast adhesion response to selective ligands for integrins $\alpha 5\beta 1$ and $\alpha v\beta 3$, which are both relevant in cancer progression, is investigated by simultaneous electrochemical impedance spectroscopy and optical microscopy. Adhesive cells on $\alpha 5\beta 1$ -selective nanopatterns showed enhanced membrane dynamics and tighter binding, compared with cells on $\alpha v\beta 3$ -selective nanopatterns. The surface of the electrode exhibits high sensitivity to small changes in surface properties, because of the constitution of specific cell-surface interactions. Moreover, such sensitivity enables differentiation between cell types. This is exemplified by analyzing distinct features in the electrochemical readout of MCF-7 breast cancer cells versus MCF-10A mammary epithelial cells, when subjected to individual adhesive nanopatches.



Cell-extracellular matrix (ECM) recognition and adhesion are central processes of the cell's sensory machinery¹ and are mediated by transmembrane adhesion receptors of the integrin family (e.g., $\alpha 5\beta 1$ and $\alpha v\beta 3$).² Upon ECM binding, integrin receptors induce different cellular signals and behaviors that are highly relevant for many pathophysiological conditions such as angiogenesis, tumor growth, osteoporosis, and cancer metastasis.³ Hence, the development of efficient early diagnosis methodologies for these conditions requires the understanding of the mechanisms underlying cell adhesion interactions. This has motivated efforts to elucidate the molecular nature of regulators of cell adhesion dynamics. In most cases, a cell and molecular biology approach, usually relying on flow cytometry and microscopy, has been the method of choice. These methods provide a great deal of detail at the molecular level, but require labeling steps and fail to provide a quantitative and unbiased understanding in real time.

Label-free noninvasive biosensing technologies, including impedance-based platforms,^{4–6} quartz microbalance,^{4,7} and evanescent wave-based optical techniques⁸ are highly appealing

for time-resolved monitoring of multiple cellular functions. Among these, electrochemical impedance-based sensors have emerged as powerful tools for the development of specific, accurate, rapid, and cost-effective point-of-care testing platforms.⁶ These devices, pioneered by Giaever and Keese,⁹ are based on AC impedance measurements using weak and noninvasive AC signals and have been successfully employed to study cellular events such as cell attachment, spreading, and motility^{10,11} through the monitoring of changes in the impedance signal in a continuous, instantaneous, and non-destructive manner. Their use as potential tools for the detection of cancer cells^{10,12} and for the screening of pharmacological agents^{13,14} has also been reported.

Most commonly used approaches for patterning ligands on conductive surfaces for such applications include continuous adherent coatings¹⁵ and nanomaterial–polymer composites,¹⁶

Received: July 14, 2017

Accepted: August 29, 2017

Published: August 29, 2017



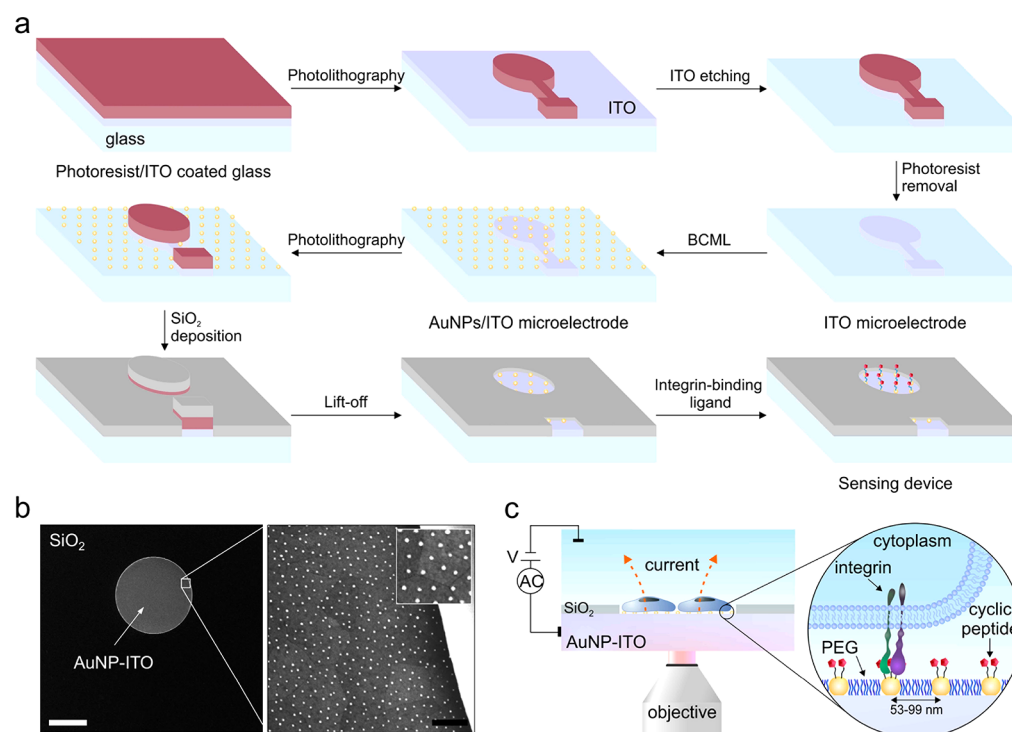


Figure 1. (a) Process sequences employed for the construction of the gold nanostructured sensors. (b) SEM micrograph showing the electroactive area of the microelectrode (center) surrounded by the SiO_2 -insulating layer (scale bar = 50 μm); the magnified section to the right shows a gold nanopattern with an interparticle spacing of 53 nm (scale bar = 200 nm). (c) Scheme of the experimental setup employed for simultaneous electrochemical and optical analysis of cell adhesion dynamics. AuNPs are functionalized with different cyclic pentapeptide ligands, as given in Table S3. The magnified section represents the interaction between the integrin extracellular domain and the ligand-coated AuNPs.

as well as self-assembled monolayers.^{14,17} A major drawback of these methods is that cellular response can only be investigated as a function of the average surface concentration of cell-adhesive ligands, making them unsuitable for interacting and measuring on length scales at which physiological adhesive events occur. Cells can sense and respond to external nanoscale features of their environment with remarkable sensitivity.¹⁸ Comprehensive studies have shown that nanoscale organization of adhesive molecules have a great influence on cell behavior.^{19–21} Therefore, electrodes tailored to mimic cellular nanoenvironments, and with the ability to transduce cellular signaling activities, would be ideal for decoding the chemical and physical cues that mediate cell-signaling pathways.

Here, we describe an approach for creating electrical impedance-based sensors that feature precisely distributed adhesive molecules for cells on their surface, while efficiently transducing cellular signaling activities. Controlled positioning of cell-anchoring sites was achieved through a quasi-hexagonal array of gold nanoparticles (AuNPs) deposited on indium tin oxide (ITO)-coated glass. The resulting electrodes exhibit well-ordered AuNPs, which not only serve as anchor points for chemical functionalization, but also maintain the superior sensitivity of nanostructured materials toward electrical transduction of surface events.

The cell dynamic response to different chemical cues, provided by either $\alpha 5 \beta 1$ - or $\alpha v \beta 3$ -integrin antagonists, acting over diverse spatial scales, was evaluated using rat embryonic fibroblasts, human breast cancer MCF-7 cells, and normal MCF-10A human breast cells. Targeting specific integrins through selective ligands patterned under geometrically controlled environments, as we describe here, constitutes a promising approach toward new nanoscale devices for cell

culture and diagnostic applications. In an exemplary analysis, nanostructured sensors functionalized with an $\alpha v \beta 3$ -integrin binding ligand were employed as a tool to differentiate MCF-7 cells from MCF-10A cells.

EXPERIMENTAL SECTION

Bioimpedance Microelectrodes. The sensing area of the electrode was delineated by a combination of photolithography and SiO_2 evaporation (Figure 1a). The positive photoresist maP1275 (Micro Resist Technology, Germany) was applied to ITO substrates by spin coating at 3000 rpm for 30 s. After a soft bake (95 $^{\circ}\text{C}$, 6 min), the substrates were subjected to ultraviolet (UV) illumination (MJB4 Mask Aligner, SUSS MicroTec, Germany) through the corresponding mask. The unexposed photoresist then was removed using maD-331 developer (Micro Resist Technology, Germany), and the substrates were rinsed with ultrapure water, dried under a nitrogen stream, and hard-baked for 30 min at 100 $^{\circ}\text{C}$. Uncovered ITO (150 nm thickness) was etched with HCl 6 M for 90 min at 20 $^{\circ}\text{C}$. The remaining photoresist was then removed using mr-Rem400 remover (Micro Resist Technology, Germany), and the substrates were rinsed with ultrapure water, dried under a nitrogen stream and patterned with AuNPs, as described in the Supporting Information. The process was repeated for the second mask. Thereafter, an insulating 500 nm SiO_2 layer was deposited on the substrates by physical vapor deposition. After removing the photoresist, the substrates were subjected to oxygen plasma treatment (80 W, 0.4 mbar, 20 min, GIGAbatch 360, PVA TePla AG, Germany). Subsequently, the area between AuNPs was passivated with mPEG-triethoxysilane (2000) to prevent nonspecific adhesion.²² Each surface was functionalized with the corresponding pentapeptide at a

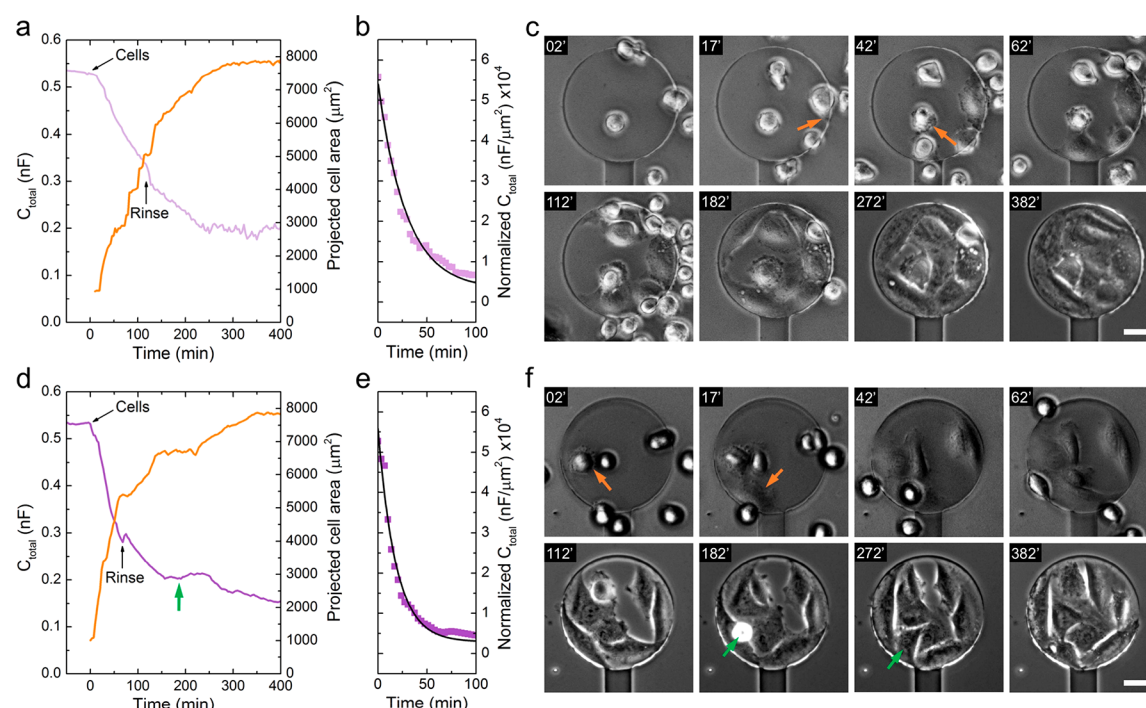


Figure 2. EIS and phase contrast microscopy monitoring of REF-52 cell adhesion dynamics on 53 nm gold nanopatterns coated with (a–c) $\alpha\text{v}\beta3$ - and (d–f) $\alpha5\beta1$ -integrin antagonist. Integrin-mediated cell adhesion was followed by capacitance (C_{total}) readings at 40 kHz (magenta trace). Projected cell area (orange trace) was obtained from the phase contrast micrographs. (b, e) A quantitative evaluation of the spreading rate was measured by following the ratio between the C_{total} and the projected cell area at different time points. Nonadhesive cells were removed by gentle rinsing. The orange arrows in the right panels indicate the early stages of cell spreading. Cell adhesion process of a single cell is highlighted with green arrows. Scale bar = 30 μm .

concentration of 25 μM in Milli-Q water for 2 h at room temperature. Physisorbed material was removed with PBS and ultrapure water. Cell adhesion experiments were carried out immediately after this step.

Dual Impedance and Microscopy. Cells were examined using an Axiovert 200 microscope (Carl Zeiss, Jena, Germany). Electrochemical impedance measurements were performed with an Autolab PGSTAT302N potentiostat (Echo Chemie, Germany), using a three-electrode configuration. Impedance spectra in the range of 10^6 – 10^1 Hz were recorded with a pure sinusoidal AC voltage of 10 mV root-mean-square (rms). The equivalent capacitance of the system was calculated from the imaginary part of the complex impedance.⁴ Capacitance readings at 40 kHz were found to be best-suited to monitor cell–substrate interactions. Cell–cell interactions were evaluated by measuring the electrode resistance at 429 Hz, corresponding to the real part of the impedance. DW-RICM measurements were performed using a microscopy system previously described.²³ Image analysis was performed with self-written Matlab scripts (Version R2010bSP1, MathWorks, Ismaning, Germany).²³

Cell Culture. Rat embryo fibroblast (REF-52) wild-type (WT) cells were a kind gift of Benjamin Geiger (Weizmann Institute of Science, Rehovot, Israel). REF-52 WT cells were cultured in DMEM medium supplemented with 10% FBS, 1% L-glutamin and 100 units/mL penicillin-streptomycin (Invitrogen, Germany) at 37 °C and 5% CO_2 . Human epithelial breast cancer cell line (MCF-7) and human epithelial normal mammary cell line (MCF-10A) were obtained from ATCC. MCF-10A cells were cultured in MEBM supplemented with MEGM Single Quots and cholera toxin (Lonza, Germany). MCF-7 cells were grown in EMEM (Lonza, Germany)

supplemented 10% FBS, 1% sodium pyruvate, 100 units/mL penicillin-streptomycin and 1% NEAA (Invitrogen, Germany). For adhesion experiments, adherent cells were removed from the culture surface by treatment with trypsin-EDTA 0.05% (Invitrogen, Germany) for 5 min at 37 °C. Cells were seeded at a density of 300 cells/ mm^2 on the respective functionalized surfaces, followed by incubation at 37 °C and 5% CO_2 in low FBS (1%)-containing media.

RESULTS AND DISCUSSION

AuNP-ITO Microelectrodes. The synthesis of optically transparent gold nanostructured electrodes with the ability to enable and transduce specific cell–ligand recognition events at precisely localized positions was conducted by diblock copolymer micelle nanolithography (see Table S1 and Figure S1 in the Supporting Information). The obtained nanostructured substrates exhibit uniform and evenly distributed Au nanoclusters, which allow control of the density of cell-binding sites with nanometer resolution, while concomitantly regulating the cell adhesion response. Moreover, this approach yielded electrically integrated AuNPs onto ITO surfaces suitable, for instance, as signal transducers of cell interactions (see Figures S2 and S3, as well as Table S2, in the Supporting Information).

Gold nanostructured microelectrodes were fabricated by a combination of photolithography and diblock copolymer micelle nanolithography, as depicted in Figure 1a. The obtained nanostructured sensors consist of a 100- μm -diameter ITO microelectrode patterned with 6.5 nm AuNPs, and surrounded by a SiO_2 -insulating layer (see Figure 1b, as well as Figures S4 and S5 in the Supporting Information). The sensor surface enables specific cell–surface interactions in well-defined

nanoscopic geometries by rendering a ligand-functionalized gold nanopattern on a nonadhesive PEG-passivated background (see Figure 1c). AuNPs were functionalized with cyclic pentapeptide ligands with different binding affinities to $\alpha 5\beta 1$ and $\alpha v\beta 3$ integrins (Table S3 in the Supporting Information). The $\alpha 5\beta 1$ -selective ligand bears a *c*(-phg-isoDGRk-) head-group,²⁴ while a *c*(-RGDfE-) based ligand was used for targeting integrin $\alpha v\beta 3$. Each ligand consists of an integrin-binding domain, a polyproline-based spacer, and a terminal thiol group for gold surface attachment (see Figure S6 in the Supporting Information). The polyproline sequence was selected as a spacer, because of its ability, more so than alkane and PEG spacers,^{25,26} to efficiently display the active moieties to the cell, thus triggering strong integrin–ligand interactions.

Electrochemical and Optical Probing of the Electrode/Cellular Interface. Multifrequency electrochemical impedance spectra (Figure S7 in the Supporting Information) were recorded during the attachment and spreading of rat embryonic fibroblast (REF-52) cells on the differently functionalized gold nanopatterned microelectrodes. Time-resolved phase contrast microscopy was performed in parallel, to provide a more-detailed overview of the cellular process. Optical inspection enables qualitative assessment of cell growth and actin-related features, which can be directly correlated to changes of electrode impedance during the cell cycle. A quantitative survey of cell–substrate interactions was conducted by capacitance readings at an AC frequency of 40 kHz. At this high frequency, the current couples capacitively through the cell membranes, collecting impedance contributions from the cell–substrate adhesion area.^{4,27} Total capacitance measurements allow the direct monitoring of the net cell surface coverage and provide sensitive and accurate means to determine the kinetics of cell spreading.²⁸ Moreover, this approach is particularly appealing for time-lapse investigation of the establishment of confluent epithelial cell cultures without the need for equivalent circuit modeling.^{4,29}

In the following, the impact of the different integrin-selective ligands on the adhesion behavior of REF-52 cells was examined by real-time monitoring of the electrode capacitance in combination with phase contrast microscopy. Figures 2a and 2d show two representative cellular activity curves of REF-52 cells on 53 nm gold nanopatterns coated with *c*(-RGDfE-) and *c*(-isoDGRk-) based ligands, respectively. It can be observed that cells seeded on the individual ligand-functionalized adhesive electrodes induce a decrease in total capacitance. This is attributed to coverage of the electrode surface by the insulating cell membrane, and it mirrors the spreading dynamics, as visualized by phase contrast microscopy (see Figures 2c and 2f, as well as Video S-1). No changes in capacitance or cell adhesion and spreading were observed when coated electrodes displaying no integrin-binding motif were exposed to cells.

After seeding the cells on the microelectrode surface, the capacitance monotonically decreased as the time increased for both coated electrodes. However, a detailed inspection of the capacitance curves reveals interesting features of the molecular cell adhesion process. On *c*(-RGDfE-) coated electrodes, cells exhibited (although briefly) a more pronounced lag time in the initiation of spreading. Then, after cell contacts were established, the overall capacitance quickly decreased during cell spreading over the electrode surface, as evidenced by the phase contrast micrographs. Conversely, cells on *c*(-isoDGRk-) sensors spread almost immediately after initial contact. REF-

52 cells plated on sensors coated with the $\alpha 5\beta 1$ -selective ligand spread faster than on *c*(-RGDfE-) coated sensors (Table 1),

Table 1. Electrochemical Impedance Parameters of the Cell Adhesive Response

substrate	selectivity (integrin)	s^a ($\times 10^5$ nF/ μm^2 min)	$\Delta C_{40\text{ kHz}}^b$ ($\times 10^5$ nF/ μm^2)
AuNP ₅₃ –ITO	$\alpha 5\beta 1$	-2.93 ± 0.26	4.93 ± 0.31
AuNP ₇₆ –ITO	$\alpha 5\beta 1$	-2.55 ± 0.32	4.71 ± 0.56
AuNP ₉₉ –ITO	$\alpha 5\beta 1$	-2.26 ± 0.21	4.45 ± 0.51
AuNP ₅₃ –ITO	$\alpha v\beta 3$	-1.95 ± 0.42	4.16 ± 0.32
AuNP ₇₆ –ITO	$\alpha v\beta 3$	-1.65 ± 0.55	4.03 ± 0.45
AuNP ₉₉ –ITO	$\alpha v\beta 3$	-1.09 ± 0.31	3.53 ± 0.31

^aDecay constant (*s*), extracted from the normalized C_{total} /time plot (Figures 2b and 2e). The data are fit to a first-order kinetic equation.

^bCapacitance difference between fully spread cells and nonadhesive cells. Values of capacitance change are normalized by the projected cell area. Data from three independent experiments are presented as mean \pm standard error of measurement (s.e.m.).

indicating that ligation of $\alpha 5\beta 1$ integrin rapidly initiates adhesive activity during cell adhesion and anchorage-dependent cell growth. This is observed in Figures 2b and 2e, where the ratio between the overall capacitance and the projected cell area is plotted versus time. These observations agree with evidence that suggests that $\alpha 5\beta 1$ and $\alpha v\beta 3$ integrins have different mechanochemical roles in establishing adhesion.^{30,31} Many studies have resorted to using ECM-based coatings, such as fibronectin (Fn) and vitronectin (Vn), to differentially engage integrins $\alpha 5\beta 1$ and $\alpha v\beta 3$, respectively.³² It has been shown that $\alpha 5\beta 1$ -mediated interactions with Fn cause enhanced cell-matrix adhesion dynamics, compared with cells using integrin $\alpha v\beta 3$ instead.^{33–36} For example, C2C12 myoblasts seeded on micrometer-size patterns coated with Fn exhibited greater numbers of adherent cells and greater cell-spreading area compared to the analogues coated with Vn.³⁴ Similar levels of cell adhesion were recently reported for REF-52 cells on Fn- and Vn-coated hydrogels of intermediate stiffness (30 kPa).³⁶ Interestingly, while all these studies have shown subtle changes between signals upon Vn- or Fn-integrin engagement, the AuNP/ITO sensor displayed improved sensitivity toward dynamic ECM-integrin binding interactions. This can be attributed to the precisely localized spatial distribution of high-affinity specific ligands achieved through the gold nanopattern. A clear display of the sensor sensitivity can be appreciated during the transduction of cell adhesion events of individual cells (green arrows, Figure 2).

The remarkable sensitivity of the nanostructured electrode toward integrin-mediated cell-matrix interactions under different environmental chemical signaling is clearly evidenced in the magnitude of the capacitance change from a cell-free to a cell-covered sensor. It is shown that not only the initial cell dynamics, but also the cell contact of surface-bound fibroblasts, are sensitively dependent on the nature of molecular recognition at cell–substrate interfaces. Cells seeded on *c*(-RGDfE-) coated sensors (Figure 2a) induced a total capacitance change of 0.32 nF for a confluent layer of cells, while this value rose to 0.39 nF (Figure 2d) when the *c*(-

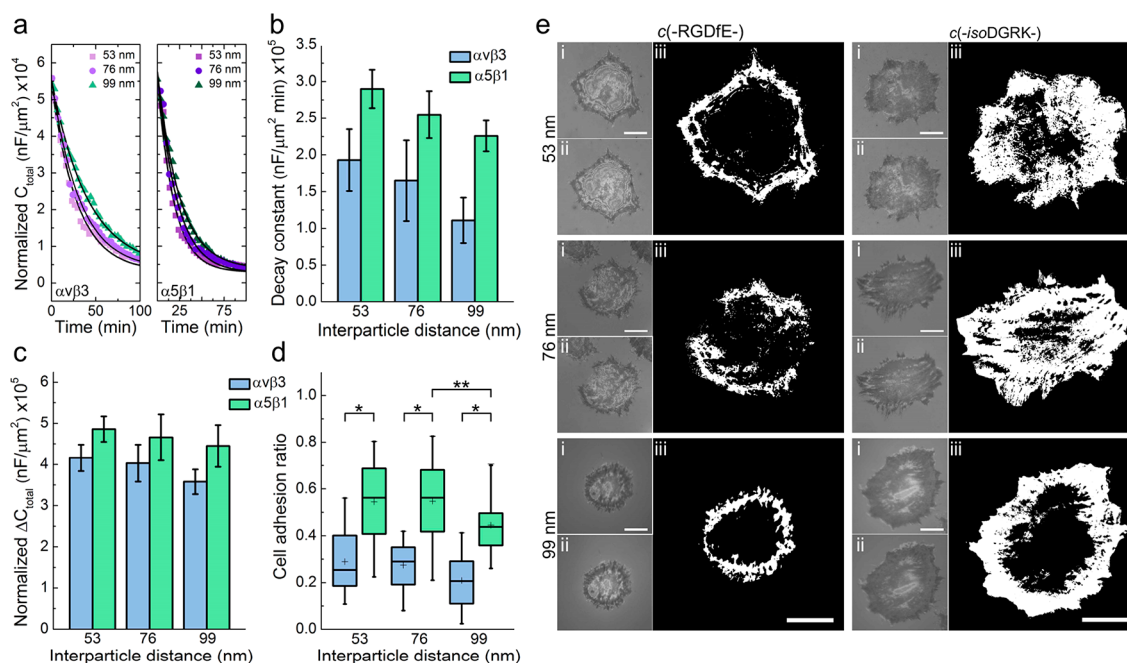


Figure 3. (a) EIS monitoring of REF-S2 cell adhesion dynamics on 53 nm (squares), 76 nm (circles), and 99 nm (triangles) gold nanopatterns coated with $\alpha\text{v}\beta3$ - and $\alpha5\beta1$ -selective peptides. Capacitance (C_{total}) readings, performed at 40 kHz, were normalized by the projected cell area and plotted against time after subtracting the lag time for spreading initiation. Data were extracted from Figure 2, as well as Figures S8 and S9. (b) Rate of capacitance change extracted from the cellular activity curves (panel (a)) and (c) capacitance difference between fully spread cells and nonadhesive cells from three independent experiments. Data are presented as mean \pm s.e.m. (d) Normalized adhesion cell area obtained from DW-RICM images, as a function of the nanopatterning conditions. At least 50 cells from at least two independent assays were analyzed. Statistical significance was determined by the Mann–Whitney test (single asterisk (*) denotes $p < 0.001$, double asterisk (**) denotes $p < 0.01$). (e) RICM images of REF-S2 cells 4 h after seeding on different gold nanopatterns ((i) 470 nm, (ii) 555 nm, and (iii) the consensus of the adhesion area observed at the two different wavelengths is shown). All areas defined as relative contact areas are represented as white areas. Scale bars correspond to 20 μm .

isoDGRk-)-based ligand mediates cell adhesion. Such results could be explained by a higher presence of dielectric structures close to the surface of the electrode, and thus a higher cell contact area for cells plated on electrodes functionalized with the $\alpha5\beta1$ -selective ligand. It is quite apparent that engagement of $\alpha5\beta1$ integrin led to significantly higher membrane dynamics, where spreading and flattening was enhanced, compared to $\alpha\text{v}\beta3$ integrin-mediated cell response.

Considering previous findings, it seems plausible to argue that the sensor is able to decode the mechanical roles of integrins in cell adhesion and spreading: $\alpha5\beta1$ integrins, which initially co-localize with $\alpha\text{v}\beta3$ -integrins at the cell edge, translocate toward the cell interior upon focal adhesions (FAs) development,³⁷ and are thought to be primarily responsible for mediating adhesion strength, while $\alpha\text{v}\beta3$ integrin is required for reinforcement and mechanotransduction. This scenario is consistent with the increase in integrin–ECM contacts for cells seeded on $\alpha5\beta1$ -selective surfaces, compared to cells on $\alpha(-\text{RGDfE-})$ -coated surfaces, as evidenced by capacitance readings, and visualized by means of dual-wavelength reflection interference contrast microscopy (DW-RICM) (vide infra). This, together with previous results, clearly shows the strong effect of engaging specific integrins on both initiation and progression of the adhesion process.

Interligand Distance Influences Cell Binding. Control over the precise spatial location of individual cell-adhesive anchoring ligands, provided by the gold nanopattern on the electrode surface, allows for the investigation of cell adhesion behavior, dependent on specific adhesive cues. In previous studies, it was shown that cells sensitively respond to variations in adhesive patch spacing above a certain threshold (~ 73

nm).^{38,39} Thus, it is reasonable to assume that alterations in cell adhesion behavior associated with changes in interligand distance may also be detected by electrochemical means. To test this assumption, REF-S2 cells were plated on $\alpha5\beta1$ - and $\alpha\text{v}\beta3$ -selective sensors featuring 76 and 99 nm interparticle distances, as similarly described for 53 nm gold nanopatterned sensors. Cell adhesion dynamics was examined in real-time by simultaneous phase contrast microscopy and EIS.

Both 76 and 99 nm gold nanopatterns, functionalized with either the $\alpha\text{v}\beta3$ - or the $\alpha5\beta1$ -integrin antagonist, supported cell adhesion and spreading, as evidenced by the decrease in total capacitance (Figure 3a) and confirmed by phase contrast visualization (Figures S8 and S9 in the Supporting Information). Cells on $\alpha5\beta1$ -selective sensors spread faster than on sensors coated with the $\alpha\text{v}\beta3$ -integrin antagonist, similar to what was observed for AuNP₅₃–ITO electrodes. Differences in spreading dynamics become more apparent as the distance between ligands increases (see Table 1 and Figure 3b). A similar trend is observed for the magnitude of the final capacitance. In agreement with previous findings,^{26,40} cell adhesive response on coated sensors strongly depends on ligand spatial organization. Cells on sensors displaying ligands at distances higher than a critical value experience a growth-limiting environment where changes in cell–ECM interactions induced by variations in adhesive chemical cues are enhanced. Interestingly, a more profound effect was observed for cells on $\alpha\text{v}\beta3$ -selective sensors, compared to those functionalized with the $\alpha5\beta1$ -selective ligand. Under a given ligand spacing of 53 nm, cells on $\alpha5\beta1$ -selective sensors exhibited a rate of capacitance change of $2.93 \times 10^{-5} \text{ nF}/\mu\text{m}^2 \text{ min}$, which is equivalent to 1.5 times the value reached on $\alpha\text{v}\beta3$ -selective

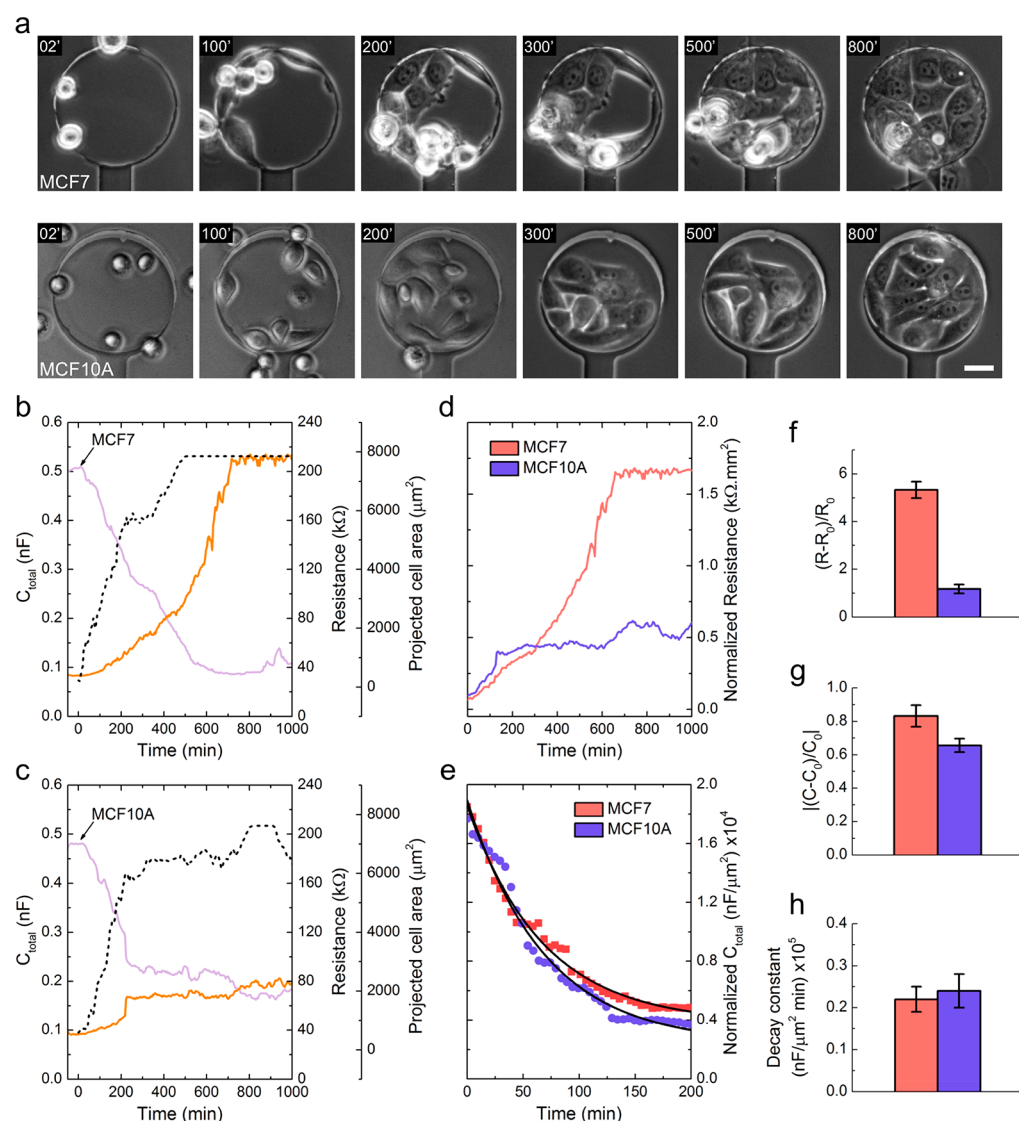


Figure 4. (a) Phase contrast microscopy and (b, c) EIS monitoring of MCF-7 and MCF-10A cell adhesion dynamics on 53 nm gold nanopatterns coated with $\alpha\beta 3$ -selective peptide. Capacitance (C_{total}) readings were acquired at 40 kHz (magenta trace). Electrode resistance was measured at 429 Hz (orange trace). Projected cell area (dotted trace) was used to normalize (d) the resistance and (e) the capacitance of the electrode. (f–h) Histograms of the evaluated parameters. Data are presented as mean \pm s.e.m. (Scale bar = 30 μm .)

sensors. This ratio increased to 2.1 when cells were seeded on 99 nm ligand-patterned sensors (Table 1). This implies that the ability of the nanostructured surface to recognize specific integrin-mediated cell adhesion processes can be tuned by manipulating the ligand nanoscale organization.

The nanostructured electrodes described herein have proved successful in mimicking the ECM and decoding cellular responses at the adhesive interface between cells and their growth support. Even subtle details of the adhesion kinetics associated with changes in the distance between the cell membrane and the surface were resolved successfully. Correlation with DW-RICM (Figures 3d and 3e), a well-established technique to visualize cell adhesion zones, supports this statement. In RICM,⁴¹ the sample is illuminated from below with parallel light and the reflected light is used for imaging. Each beam of light is reflected partially at the glass/medium interface and at the basal cell membrane. Interference between reflected light beams provides a contrast that maps the cell contact area, which are observed as dark areas. We employed multiwavelength RICM to avoid the ambiguities of

single wavelength due to the varying refractive indices in different parts of the cell.²³ We found remarkable agreement between DW-RICM and EIS results. As evident from the interferograms (Figure 3e), REF-52 cells seeded on *c*-(RGDfE)-coated surfaces, compared to cells on $\alpha 5\beta 1$ -selective surfaces, showed significantly lower adhesion area (Figure 3d). Interestingly, adhesion zones within the cells are distributed differently, depending on the surface coating. Adhesion zones in cells interacting with the $\alpha\beta 3$ -integrin antagonist exhibited a peripheral distribution, while adhesion zones in cells plated on *c*-(isoDGRk-) were distributed more evenly over the entire cellular contact zone. These observations agree with the roles attributed to $\alpha 5\beta 1$ and $\alpha\beta 3$ integrins,³⁰ and they confirm our previous interpretation based on capacitance readings.

Differentiation between Cell Types: MCF-7 vs MCF-10A. The ability of this nanostructured sensing platform to differentiate between cell types was evaluated with MCF-7 human breast cancer cells and MCF-10A human breast epithelial cells. Cell adhesion studies were conducted on sensors displaying *c*-(RGDfE-) moieties on 53 nm gold

nanopatterns. As described for REF-52 cell studies, adhesion of MCF-7 and MCF-10A cells was monitored in real-time by simultaneous phase contrast microscopy and EIS (see [Figure S10](#) in the Supporting Information). [Figure 4](#) summarizes the characteristics of the two cell behaviors.

[Figure 4a](#) shows the progression of cell adhesion and proliferation over time until the entire surface of the electrode is covered by cells, indicating the successful establishment of integrin–ligand interactions. As can be seen by the micrograph sequences, MCF-7 cells remained close to each other, spreading together as a unit, while MCF-10A cells exhibited higher mobility, and transiently separate during cell spreading (see [Video S-2](#)). These observations suggest differences in terms of cell–cell interactions between cell types. Interestingly, electrochemical impedance measurements as shown in [Figures 4b](#) and [4c](#) provided quantitative, valuable information on the establishment of these intercellular contacts. Changes in electrode resistance (orange trace), measured at a frequency of 429 Hz were acquired during the spreading of MCF-7 and MCF-10A cells. Within the low-frequency range, the current flows through the gap between adjacent cells into the bulk electrolyte.⁴ At 429 Hz, impedance readings were found to be sensitive to the formation of cell–cell junctions, with only minor effect from cell–substrate interactions.

As MCF-7 cells adhere and spread on the coated sensor, an increase in resistance is detected, which reflects the evolution of the projected cell area (dotted trace) and mirrors the change in capacitance (magenta trace). However, after cells covered the entire sensor area, resistance continued to increase, at an even higher rate than before, covering the entire sensor, until reaching a steady value. These changes in resistance during the latter time course of cell adhesion can be attributed to the assembly of adherens junctions. Conversely, MCF-10A exhibited a moderate increase in resistance as the projected cell area increased during the entire time course of the measurement. The differences between cell types become even more evident when the resistance normalized by the projected cell area is plotted as a function of time ([Figure 4d](#)). These findings correlate well with studies comparing the expression levels of biomarkers associated with cancer invasion and metastasis.^{42–44} Human breast cancer cells of luminal subtype, such as MCF-7 cells, are characterized by increased adhesive properties due to the high level of E-cadherin expression,⁴⁵ whereas MCF-10A cells express a lower level of E-cadherin.⁴⁴ Furthermore, MCF-10A cells exhibit significant invasive activity in contrast with MCF-7 cells, as evidenced in an invasion assay across a Matrigel barrier.⁴² In other words, the combination of higher mobility and lower density of cell–cell contacts of MCF-10A vs MCF-7 cells results in spaces between cells that are not tight enough to effectively limit current from flowing to the bulk phase.

Cell–substrate interactions, measured as changes in electrode capacitance ([Figures 4b](#) and [4c](#)), also differed between cell types. A sensor covered with MCF-7 cells experienced a total capacitance change of 0.42 nF, whereas the capacitance drop on electrodes covered with MCF-10A cells was 25% smaller ([Figure 4g](#)). Given that MCF-10A cells express $\alpha v \beta 3$ integrins, which are not expressed by MCF-7 cells, the opposite results would have been expected. However, it should be noted that MCF-7 cells are rich in $\alpha v \beta 5$ integrin,⁴⁶ which is a potential donor of the αv subunit, which can also mediate adhesion to c(RGDfE)-coated nanopatterns.⁴⁷ Cell–cell interactions also influence capacitance readings. The lower

capacitance observed for MCF-7 cells correlates with tight intercellular junctions.²⁸ Moreover, the biomechanical properties of these cell lines should be taken into consideration. MCF-7 cells have lower stiffness, compared to MCF-10A cells.⁴⁸ As a result, MCF-7 cells are more susceptible to deformation, which, in turn, can lead to a greater decrease in electrode capacitance. Although the latter seems to have an important influence on the electrochemical response, more-detailed studies on integrin-mediated cell adhesion and spreading should be conducted in order to obtain a more complete view of this phenomenon. The complexity of the cell–substrate interactions is also reflected in the longer lag time observed during MCF-10A cell adhesion and spreading in comparison to MCF-7 cells ([Video S-2](#)). Nevertheless, these differences observed in the initial stage of cell attachment do not correlate with the adhesion dynamics, as shown in [Figures 4e](#) and [4h](#), where no significant differences were observed between cell types.

■ CONCLUSIONS

We have successfully used diblock copolymer micelle nanolithography to pattern nanoscale arrays of ordered AuNPs onto ITO substrates with dimensions that match the length scale relevant for cell–matrix interactions. These structures provide integrin-selective adhesion sites for cells at controlled distances by rendering either $\alpha 5 \beta 1$ - or $\alpha v \beta 3$ -integrin specific antagonists. This feature, together with the proper electrical connection of the gold dots to the probing electrode, create an ideal combination for evaluating individual contributions of integrins to the cell adhesion processes via electrochemical means. REF-52 cells interacting with $\alpha 5 \beta 1$ -selective surfaces exhibit faster adhesion dynamics and a higher density of cell–matrix contacts, compared to cells seeded on $\alpha v \beta 3$ -selective surfaces. The ability of the sensing device to trigger specific cell adhesion responses and to transduce such events can be further tuned by simply adjusting the distance between binding domains. In addition, the optical transparency of the electrodes allows for simultaneous characterization by optical microscopy techniques. The sensor is suitable for distinguishing malignant cells from healthy cells based on cell–substrate and cell–cell interactions. MCF-7 human breast cancer cells were differentiated from nontumorigenic MCF-10A human breast epithelial cells, using a sensor functionalized with a cRGD-based binding ligand. Electrode capacitance, as a way to evaluate cell–substrate interactions, is influenced by the biomechanical properties of the cells and the expression profiles of specific integrins. At low frequency, high electrode resistance correlates with high density of adherens junctions, as observed for MCF-7 cells, in comparison with MCF-10A. Together, the monitoring of these parameters serves as a powerful tool for the identification of specific cells. Clearly, these sensing devices interpret the cellular response to environmental signaling, thus providing a promising approach for studying the effects of specific spatial and chemical cues on cellular functions, thereby paving the way toward cell pathology diagnostic applications.

■ ASSOCIATED CONTENT

● Supporting Information

The Supporting Information is available free of charge on the ACS Publications website at DOI: [10.1021/acs.analchem.7b02743](https://doi.org/10.1021/acs.analchem.7b02743).

Methodology used, characterization of nanostructured substrates, binding peptides data, additional EIS and phase contrast microscopy monitoring of REF52, MCF-7, and MCF-10A cells on nanostructured sensors (PDF) Movie of REF-52 cells on AuNP₅₃-ITO substrates (MPG)

Movie of MCF-10A and MCF-7 cells on AuNP₅₃-ITO substrates (MPG)

AUTHOR INFORMATION

Corresponding Author

*E-mail: dpallarola@unsam.edu.ar.

ORCID

Diego Pallarola: 0000-0001-5063-4288

Notes

The authors declare no competing financial interest.

ACKNOWLEDGMENTS

D.P. acknowledges financial support from Max-Planck-Gesellschaft (Max Planck Partner Group Nanoelectronics for Cellular Interfaces INS/MPI-MR). Parts of the research leading to these results have received funding from the European Union Seventh Framework Programme (FP7/2007–2013), under Grant Agreement Nos. NMP4-LA-2009-229289 NanoII and NMP3-SL-2009-229294 NanoCARD, as well as from an ERC Advanced Grant, under Grant Agreement No. 294852-SynAd. The authors acknowledge the support of the excellence cluster CellNetworks at the University of Heidelberg. J.P.S. acknowledges the support from DFG SFB 1129 (P1 and P15). D.P. is staff researcher of CONICET. J.P.S. is the Weston Visiting Professor at the Weizmann Institute of Science. The Max Planck Society is appreciated for its general support in all aspects of our research.

REFERENCES

- (1) Yao, X.; Peng, R.; Ding, J. D. *Adv. Mater.* **2013**, *25*, 5257–5286.
- (2) Cox, D.; Brennan, M.; Moran, N. *Nat. Rev. Drug Discovery* **2010**, *9*, 804–820.
- (3) Luo, B. H.; Carman, C. V.; Springer, T. A. *Annu. Rev. Immunol.* **2007**, *25*, 619–647.
- (4) Janshoff, A.; Kunze, A.; Michaelis, S.; Heitmann, V.; Reiss, B.; Wegener, J. J. *Adhes. Sci. Technol.* **2010**, *24*, 2079–2104.
- (5) Hong, J.; Kandasamy, K.; Marimuthu, M.; Choi, C. S.; Kim, S. *Analyst* **2011**, *136*, 237–245.
- (6) Xu, Y.; Xie, X.; Duan, Y.; Wang, L.; Cheng, Z.; Cheng, J. *Biosens. Bioelectron.* **2016**, *77*, 824–836.
- (7) Ben Ishay, R.; Kapp-Barnea, Y.; Grigoriantz, I.; Teblum, E.; Lellouche, J.-P. *Sens. Actuators, B* **2015**, *215*, 373–381.
- (8) Malachovska, V.; Ribaut, C.; Voisin, V.; Surin, M.; Leclerc, P.; Wattiez, R.; Caucheteur, C. *Anal. Chem.* **2015**, *87*, 5957–5965.
- (9) Giaever, I.; Keese, C. R. *Proc. Natl. Acad. Sci. U. S. A.* **1991**, *88*, 7896–7900.
- (10) Arias, L. R.; Perry, C. A.; Yang, L. *Biosens. Bioelectron.* **2010**, *25*, 2225–2231.
- (11) Susloparova, A.; Koppenhoefer, D.; Law, J. K. Y.; Vu, X. T.; Ingebrandt, S. *Lab Chip* **2015**, *15*, 668–679.
- (12) Abdolabad, M.; Shashaani, H.; Janmaleki, M.; Mohajerzadeh, S. *Biosens. Bioelectron.* **2014**, *59*, 151–159.
- (13) Ramasamy, S.; Bennet, D.; Kim, S. *Int. J. Nanomed.* **2014**, *9*, 5789–5809.
- (14) Parviz, M.; Gaus, K.; Gooding, J. J. *Chem. Sci.* **2017**, *8*, 1831–1840.
- (15) Choi, Y.; Yagati, A. K.; Cho, S. J. *Nanosci. Nanotechnol.* **2015**, *15*, 7881–7885.
- (16) Kim, T. H.; El-Said, W. A.; An, J. H.; Choi, J. W. *Nanomedicine* **2013**, *9*, 336–344.
- (17) Wang, L.; Zhu, J.; Deng, C.; Xing, W.-L.; Cheng, J. *Lab Chip* **2008**, *8*, 872–878.
- (18) Murphy, W. L.; McDevitt, T. C.; Engler, A. J. *Nat. Mater.* **2014**, *13*, 547–557.
- (19) Deeg, J. A.; Louban, I.; Aydin, D.; Selhuber-Unkel, C.; Kessler, H.; Spatz, J. P. *Nano Lett.* **2011**, *11*, 1469–1476.
- (20) Li, S.; Wang, X.; Cao, B.; Ye, K.; Li, Z.; Ding, J. *Nano Lett.* **2015**, *15*, 7755–7765.
- (21) Ye, K.; Wang, X.; Cao, L. P.; Li, S. Y.; Li, Z. H.; Yu, L.; Ding, J. D. *Nano Lett.* **2015**, *15*, 4720–4729.
- (22) Platzman, I.; Muth, C. A.; Lee-Thedieck, C.; Pallarola, D.; Atanasova, R.; Louban, I.; Altmann, E.; Spatz, J. P. *RSC Adv.* **2013**, *3*, 13293–13303.
- (23) Munding, T. A.; Sommerfeld, A.; Reinehr, R.; Spatz, J. P.; Hauessinger, D.; Boehm, H. *PLoS One* **2012**, *7*, DOI: 10.1371/journal.pone.0048100.
- (24) Bochen, A.; Marelli, U. K.; Otto, E.; Pallarola, D.; Mas-Moruno, C.; Di Leva, F. S.; Boehm, H.; Spatz, J. P.; Novellino, E.; Kessler, H.; Marinelli, L. *J. Med. Chem.* **2013**, *56*, 1509–1519.
- (25) Pallarola, D.; Bochen, A.; Boehm, H.; Rechenmacher, F.; Sobahi, T. R.; Spatz, J. P.; Kessler, H. *Adv. Funct. Mater.* **2014**, *24*, 943–956.
- (26) Pallarola, D.; Platzman, I.; Bochen, A.; Cavalcanti-Adam, E. A.; Axmann, M.; Kessler, H.; Geiger, B.; Spatz, J. P. *BioNanoMat* **2017**, *18*, 20160014.
- (27) Gheorghiu, E.; Balut, C.; Gheorghiu, M. *Phys. Med. Biol.* **2002**, *47*, 341–348.
- (28) Wegener, J.; Keese, C. R.; Giaever, I. *Exp. Cell Res.* **2000**, *259*, 158–166.
- (29) Michaelis, S.; Wegener, J.; Robelek, R. *Biosens. Bioelectron.* **2013**, *49*, 63–70.
- (30) Schiller, H. B.; Hermann, M.-R.; Polleux, J.; Vignaud, T.; Zanivan, S.; Friedel, C. C.; Sun, Z.; Raducanu, A.; Gottschalk, K.-E.; Thery, M.; Mann, M.; Faessler, R. *Nat. Cell Biol.* **2013**, *15*, 625–636.
- (31) Rahmouni, S.; Lindner, A.; Rechenmacher, F.; Neubauer, S.; Sobahi, T. R. A.; Kessler, H.; Cavalcanti-Adam, E. A.; Spatz, J. P. *Adv. Mater.* **2013**, *25*, 5869–5874.
- (32) Goodman, S. L.; Picard, M. *Trends Pharmacol. Sci.* **2012**, *33*, 405–412.
- (33) Truong, H.; Danen, E. H. J. *Cell Adh. Migr.* **2009**, *3*, 179–181.
- (34) Malmstrom, J.; Lovmand, J.; Kristensen, S.; Sundh, M.; Duch, M.; Sutherland, D. S. *Nano Lett.* **2011**, *11*, 2264–2271.
- (35) Stachurska, A.; Elbanowski, J.; Kowalczyńska, H. M. *Cell Biol. Int.* **2012**, *36*, 883–892.
- (36) Missirlis, D.; Spatz, J. P. *Biomacromolecules* **2014**, *15*, 195–205.
- (37) Morgan, M. R.; Byron, A.; Humphries, M. J.; Bass, M. D. *IUBMB Life* **2009**, *61*, 731–738.
- (38) Cavalcanti-Adam, E. A.; Volberg, T.; Micoulet, A.; Kessler, H.; Geiger, B.; Spatz, J. P. *Biophys. J.* **2007**, *92*, 2964–2974.
- (39) Wang, X.; Li, S.; Yan, C.; Liu, P.; Ding, J. *Nano Lett.* **2015**, *15*, 1457–1467.
- (40) Arnold, M.; Schwieder, M.; Blümmel, J.; Cavalcanti-Adam, E. A.; López-García, M.; Kessler, H.; Geiger, B.; Spatz, J. P. *Soft Matter* **2009**, *5*, 72–77.
- (41) Limozin, L.; Sengupta, K. *ChemPhysChem* **2009**, *10*, 2752–2768.
- (42) Gordon, L. A.; Mulligan, K. T.; Maxwell-Jones, H.; Adams, M.; Walker, R. A.; Jones, J. L. *Int. J. Cancer* **2003**, *106*, 8–16.
- (43) Subik, K.; Lee, J. F.; Baxter, L.; Strzepek, T.; Costello, D.; Crowley, P.; Xing, L.; Hung, M. C.; Bonfiglio, T.; Hicks, D. G.; Tang, P. *Breast Cancer (Auckland)* **2010**, *4*, 35–41.
- (44) Chekhun, S.; Bezdenezhnykh, N.; Shvets, J.; Lukianova, N. *Exp. Oncol.* **2013**, *35*, 174–179.
- (45) van Roy, F.; Berx, G. *Cell. Mol. Life Sci.* **2008**, *65*, 3756–3788.
- (46) Taherian, A.; Li, X.; Liu, Y.; Haas, T. A. *BMC Cancer* **2011**, *11*, 293.
- (47) Kapp, T. G.; Rechenmacher, F.; Neubauer, S.; Maltsev, O. V.; Cavalcanti-Adam, E. A.; Zarka, R.; Reuning, U.; Notni, J.; Wester, H.

J.; Mas-Moruno, C.; Spatz, J.; Geiger, B.; Kessler, H. *Sci. Rep.* **2017**, *7*, 39805.

(48) Geltmeier, A.; Rinner, B.; Bade, D.; Meditz, K.; Witt, R.; Bicker, U.; Bludszweit-Philipp, C.; Maier, P. *PLoS One* **2015**, *10*, e0134999.